https://doi.org/10.5194/egusphere-2025-1031
Preprint. Discussion started: 23 April 2025

Atmospheric and watershed modelling of HFO-1234ze(E) emissions from prospective pressurized metered-dose inhalers usage

Shivendra G. Tewari[1], Krish Vijayaraghavan[2], Kun Zhao[2], Liji M. David[2], Katie Tuite[2], Felix Kristanovich[2], Yuan Zhuang[2], Benjamin Yang[2], Cecilia Hurtado[2], Dimitrios K. Papanastasiou[3], Paul Giffen[4], Holly Kimko[1], Megan Gibbs[1], Stefan Platz[5]

[1]Clinical Pharmacology & Quantitative Pharmacology, R&D BioPharmaceuticals, AstraZeneca, Gaithersburg, USA
[2]Ramboll, Novato, USA
[3]Honeywell, Buffalo, USA
[4]Clinical Pharmacology & Safety Sciences, R&D BioPharmaceuticals, AstraZeneca, Cambridge, UK
[5]Clinical Pharmacology & Safety Sciences, R&D BioPharmaceuticals, AstraZeneca, Baar, Switzerland

Correspondence to: Shivendra G. Tewari (shivendra.tewari@astrazeneca.com)

Abstract. HFO-1234ze(E) is a next-generation medical propellant in development for use in pressurized metered-dose inhalers (pMDIs). The chemical structure of HFO-1234ze(E) has the '–CF_3' moiety, which makes formation of trifluoroacetic acid (TFA) possible in the atmosphere. To quantify the contribution of these novel pMDIs in forming environmental TFA, we performed an extensive study using a global atmospheric model coupled with detailed watershed modelling. Herein, we included the master-chemical mechanism of HFO-1234ze(E), accounting for all known pathways that may form atmospheric TFA and assumed pMDI usage as the only source of HFO-1234ze(E) emissions. Based on annual pMDI sales data and HFO-1234ze(E) as their sole medical propellant, we estimate annual global propellant emissions of 4.736 Gg/year. Even though pMDI sales are the highest in regions within the northern-temperate zone, model-predicted TFA deposition rates are higher in regions within the tropical zone, suggesting that photolysis reaction of trifluoroacetic aldehyde (TFAA; which does not yield TFA) is dominant in the northern-temperate zone. We used model-predicted TFA deposition rates around the Hudson River, Cauvery River, and Rhine River as an input to our fate-and-transport model of TFA, yielding pMDI usage-based TFA concentrations in surface water, soil and sediments in each of the three modelled watersheds. Our watershed models predict that TFA concentrations in river surface water would vary between 0.8–19.3 ng/L, indicating greater than 500-fold margin-of-exposure for drinking-water TFA. Our results demonstrate that environmental TFA formation due to pMDI usage-based HFO-1234ze(E) emissions do not pose a human health concern.

1 Introduction

Asthma and Chronic obstructive pulmonary disease (COPD) are potentially life-threatening diseases, affecting roughly half a billion people globally and cause nearly 4 million deaths each year (Collaborators, 2020). Patients living with respiratory diseases generally rely on pressurized metered dose inhalers (pMDIs), dry powder inhalers, or soft-mist inhalers for treatment of these conditions. Of these options, pMDIs are the most prescribed devices globally with greater than 90% usage

https://doi.org/10.5194/egusphere-2025-1031
Preprint. Discussion started: 23 April 2025

in some countries (Bell et al., 2023). pMDI devices rely on a medical propellant for delivering the active pharmaceutical ingredient (API) to a patient's lungs. Present-day pMDI devices use hydrofluorocarbons (HFCs) as the medical propellant; however, all HFC-based propellants have high global warming potential (GWP), e.g., HFC-134a has a GWP (100-year time horizon) that is 1,430 times greater than CO_2 (Masson-Delmotte and Matthews, 2021), and are subject to phase down under the Kigali amendment of the Montreal Protocol (Heath, 2017). The American Innovation and Manufacturing (AIM) Act, enacted by Congress in 2020, authorized US Environmental Protection Agency (EPA) to phase down the production and consumption of hydrofluorocarbons, such as HFCs, by 2036 (Logan, 2021).

To ensure supply of these essential medications to patients, the pharmaceutical industry has developed a near-zero GWP medical propellant (Tewari et al., 2023), trans-1,3,3,3-tetrafluoroprop-1-ene (the E-isomer), correctly written as E-CF_3CH=CHF or HFO-1234ze(E) or next-generation medical propellant (NGP) (a hydrofluoroolefin; HFO), with initial pMDI devices expected to transition this year and transition of all pMDI devices anticipated by 2030. According to the Organization for Economic Cooperation and Development (OECD) definition, HFO-1234ze(E) belongs to a group of synthetic chemicals called per- and polyfluoroalkyl substances (PFAS) which are typically resistant to environmental breakdown. PFAS are a group of nearly 15,000 chemicals (Williams et al., 2017) with substantially diverse physicochemical properties, e.g., HFO-1234ze(E) upon release in the atmosphere breaks down within ~20 days (Tewari et al., 2023; Neale et al., 2021) while some PFAS can take many years to decompose. Despite the diverse structure and behaviour of PFAS chemicals, in 2023, five European Union (EU) countries submitted a blanket-restriction proposal under the Registration, Evaluation, Authorisation and Restriction of Chemicals (REACH) banning all manufacturing and usage of PFAS in the EU with exceptions for human and veterinary APIs, biocides, pesticides, and a few fully degradable PFAS subgroups.

HFO-1234ze(E) falls under the purview of the PFAS-restriction proposal because its structure contains a trifluoromethyl group (–CF_3) which makes formation of trifluoroacetic acid (TFA) possible in the atmosphere; TFA is the most abundant PFAS in the environment (Arp et al., 2024); presently, there are nearly 2,000 chemicals that have the potential of forming TFA in the environment (Adlunger et al., 2021). The atmospheric chemistry of HFO-1234ze(E) has been the subject of a few past studies and is relatively well understood (Søndergaard et al., 2007; Javadi et al., 2008; Burkholder et al., 2015b). HFO-1234ze(E) primarily interacts with OH radicals in the atmosphere, leading to the formation of trifluoroacetic aldehyde (TFAA) as the main product (Javadi et al., 2008; Burkholder et al., 2015b). TFAA is mainly eliminated from the atmosphere through photolysis, a process that does not result in the formation of TFA (Tewari et al., 2023). However, it has been suggested that the OH-initiated TFAA atmospheric degradation and the subsequent reaction of the corresponding peroxy radicals with HO_2 radicals can lead to TFA formation (Sulbaek Andersen et al., 2004). In addition, several other TFAA degradation pathways have been suggested in the literature (Pérez-Peña et al., 2023; Long et al., 2022; Andersen and Nielsen, 2022) which, ultimately, can affect the overall atmospheric chemistry of HFO-1234ze(E) and therefore its potential to form TFA. To the best of our knowledge, there is no prior work that explored the formation of TFA from HFO-1234ze(E) utilizing a global chemical transport modelling. Lastly, provided that any TFA formed from the atmospheric degradation of

https://doi.org/10.5194/egusphere-2025-1031
Preprint. Discussion started: 23 April 2025

fluorinated gases is, eventually, deposited on Earth's surface via wet and dry deposition, it is also important to evaluate its fate and transport in surface soil and water media, upon deposition.

We therefore performed a state-of-the-art study coupling global chemical transport modelling with TFA surface fate and transport modelling to estimate surface water, sediment, and surface soil concentrations of TFA over a period of 30 years due to continued, global sales of prospective pMDIs using only HFO-1234ze(E) as the medical propellant. Lastly, we compared our estimates of environmental TFA production due to pMDI usage with that from all other sources.

2 Methods

2.1 Software

We applied a global three-dimensional chemical transport model, GEOS-Chem (version 14.2.2, https://doi.org/10.5281/zenodo.10034733), driven by meteorological data assimilated from the Goddard Earth Observing System (GEOS) at the National Aeronautics and Space Administration (NASA) Global Modeling and Assimilation Office. The model incorporates a detailed mechanism for oxidant-aerosol chemistry computed within the troposphere and the stratosphere at 30 minute time intervals using a fourth-order Rosenbrock kinetic solver implemented with the Kinetic preprocessor version 3.0 (Lin et al., 2023). Emissions were calculated at 30 minute time steps using the Harmonized Emissions Component (HEMCO) module version 3.0 (Lin et al., 2021).

In this study, GEOS-Chem was configured to use modern-era retrospective analysis for research and applications, version 2 (MERRA-2) reanalysis meteorology data with varying temporal resolutions: 3-hourly for three-dimensional fields, such as wind components (zonal wind and meridional wind) and temperature, and hourly for surface variables and mixing depths, including soil moisture, heat fluxes, and albedo (Gelaro et al., 2017). We conducted the global modeling at a 2°×2.5° resolution across 47 vertical 'eta' levels from the surface to approximately 80 km; here, 'eta' refers to vertical levels in hybrid sigma-pressure coordinates. Additionally, the horizontal resolution of the meteorological fields was updated to align with the 2°×2.5° grid of the model. The wet deposition of aerosols and soluble gases by precipitation includes the scavenging in convective updrafts, in-cloud rainout, and below-cloud washout (Liu et al., 2001). The dry deposition was calculated using a resistance-in-series parameterization, which is dependent on environmental variables and lookup table values (Wesely, 2007). To obtain initial concentrations, model spin-up simulations were performed at 4°×5° grid resolution for approximately eight years until the concentrations of species varied little from one year to the next. The final simulations were performed at 2°×2.5° resolution for the year 2022.

2.2 Anthropogenic and Natural emissions

The global anthropogenic emissions are from the Community Emissions Data System (CEDS version 2) inventory for 1980-2019 at 0.1°×0.1° resolution (Hoesly et al., 2018). They include chemically reactive gases (sulfur dioxide (SO_2), nitrogen oxides (NO_x), ammonia (NH_3), methane (CH_4), carbon monoxide (CO), and non-methane volatile organic compounds

https://doi.org/10.5194/egusphere-2025-1031
Preprint. Discussion started: 23 April 2025

(NMVOCs)), carbonaceous aerosol (black carbon (BC) and organic carbon (OC)), and carbon dioxide (CO_2). Emissions are provided on an annual basis at the level of country and sector, with a monthly temporal resolution. The CEDS inventory includes emissions from ships for all species included in the inventory and is used as the global ship emissions inventory in the model. Ethane emissions were from Tzompa-Sosa et al. (Tzompa-Sosa et al., 2017) and propane emissions from Xiao et al. (Xiao et al., 2008). Aircraft emissions are from the AEIC 2019 inventory (Simone et al., 2013). The monthly-averaged 0.25°×0.25° biomass burning emissions were obtained from the Global Fire Emissions Database version 4 (GFED4, (Van Der Werf et al., 2017)). The biogenic volatile organic compounds emissions were derived from the Model of Emissions of Gases and Aerosols from Nature (MEGAN) version 2.1 (Guenther et al., 2012), as implemented by Hu et al. (Hu et al., 2015), and calculated offline to improve reproducibility across scales (Weng et al., 2020). The mineral dust emissions were calculated offline at native meteorological resolution using the Dust Entrainment and Deposition scheme of Zender et al. (Zender et al., 2003), combined with an updated high-resolution dust source function (Meng et al., 2020). Sea salt emissions from the open ocean are dependent on wind speed and sea surface temperature, and follow the algorithm of Jaegle et al. (Jaeglé et al., 2011). The algorithm for above-canopy soil NO_x emissions follows Hudman et al. (Hudman et al., 2012), with the efficiency of loss to the canopy depending on vegetation type and density. Emissions from other natural sources (e.g., lightning and volcanoes) were also included (Carn et al., 2015; Murray et al., 2012).

2.3 HFO-1234ze(E) degradation mechanism

The standard GEOS-Chem model uses a set of chemical mechanisms implemented with a kinetic preprocessor. The model includes aerosol chemistry and stratospheric chemistry (Eastham et al., 2014), and reaction rates and products are based on NASA Jet Propulsion Laboratory (JPL) Panel for Data Evaluation or the International Union of Pure and Applied Chemistry (IUPAC) Task Group on Atmospheric Chemical Kinetic Data Evaluation recommendations (Burkholder et al., 2015a; Sander et al., 2006; Sander et al., 2010). Photolysis frequencies are calculated with the Fast-JX code (version 7.0) (Bian and Prather, 2002) as implemented in GEOS-Chem by Mao et al. (Mao et al., 2010) for the troposphere and by Eastham et al. (Eastham et al., 2014) for the stratosphere. There are a total of 921 reactions, including 104 photolysis reactions, in the model.

A detailed gas phase degradation mechanism for HFO-1234ze(E) has been constructed, in a format that is compatible with that used in the Master Chemical Mechanism, MCM (Jenkin et al., 1997; Jenkin et al., 2003; Jenkin et al., 2015; Saunders et al., 2003). The mechanism makes use of published kinetic and mechanistic information relevant to HFO-1234ze(E) degradation and, where possible, applies parameters recommended either by the IUPAC https://iupac.aeris-data.frhttp://jpldataeval.jpl.nasa.gov/or the JPL. Where no information is available, kinetic parameters and product channel contributions are estimated using published estimation methods (e.g., Jenkin et al., (Jenkin et al., 2018; Jenkin et al., 2019); Kwok and Atkinson, (Kwok and Atkinson, 1995)) or assigned by analogy with chemistry reported for structurally similar species. Figure 1 shows the full mechanism, which contains 68 reactions. Table S1 of the Supplement describes these reactions and the origin of the assigned kinetic parameters. To reduce the computational burden of the GEOS-Chem model,

https://doi.org/10.5194/egusphere-2025-1031
Preprint. Discussion started: 23 April 2025

we have simplified the mechanism to twenty-nine reactions, including four photolysis reactions and reactions associated with TFA formation. We have excluded some atmospheric species, such as O_2 and H_2O, from the chemical reactions since concentrations of these species are relatively stable and including them explicitly in every chemical reaction can add unnecessary complexity without significantly improving the model accuracy.

The first step is the hydroxyl radical (OH)-initiated oxidation of $CF_3CH=CHF$, represented by a single reaction in GEOS-Chem (Tewari et al., 2023):

$$CF_3CHCHF + OH \rightarrow FRO_2 \quad \text{(R1)}$$

Here, FRO_2 denotes the peroxy-radicals $CF_3CH(OH)CH(O_2)F$ and $CF_3CH(O_2)CH(OH)F$. The rate constant for reaction R1 is from the IUPAC (Ammann et al., 2016). The peroxy radical from reaction R1 reacts with NO and HO_2. The reaction with NO generates 2,2,2-

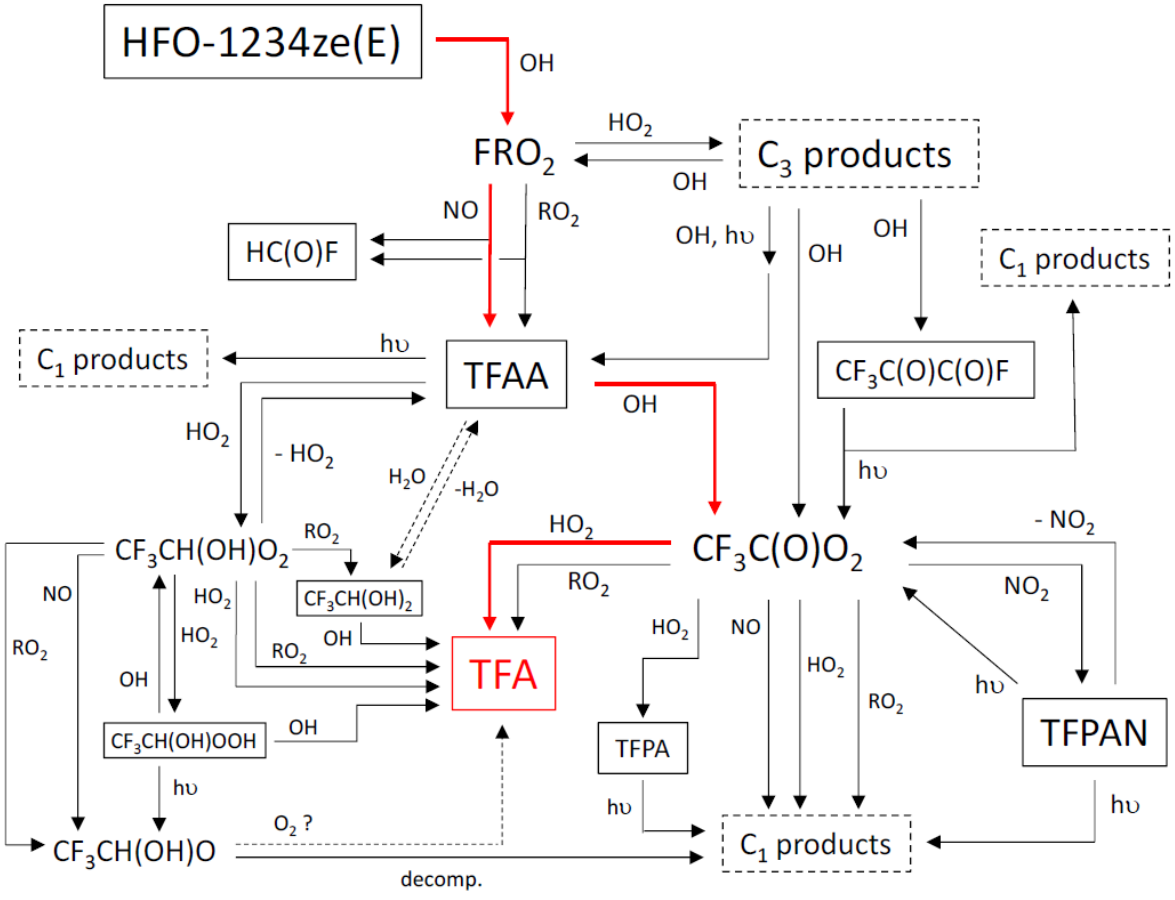

Figure 1: Schematic of gas-phase degradation mechanism for HFO-1234ze(E). The red arrows show the primary route for TFA (trifluoroacetic acid, $CF_3C(O)OH$) formation. Abbreviations: FRO_2, peroxy radicals $CF_3CH(OH)CH(O_2)F$ and $CF_3CH(O_2)CH(OH)F$; TFAA, trifluoroacetic aldehyde; TFPAN, trifluoracetyl peroxy nitrate; TFPA, trifluoroperacetic acid; and C3 products, $CF_3CH(OH)CH(OOH)F$, $CF_3CH(OOH)CH(OH)F$, $CF_3CH(OH)C(O)F$ and $CF_3C(O)CH(OH)F$.

https://doi.org/10.5194/egusphere-2025-1031
Preprint. Discussion started: 23 April 2025

trifluoroacetic aldehyde (TFAA; CF_3CHO) and formyl fluoride (HCOF), while its reaction with HO_2 forms a hydroxy-carbonyl product, $CF_3CH(OH)C(O)F$:

$$FRO_2 + NO \rightarrow CF_3CHO + HCOF + HO_2 + NO_2 \quad (R2)$$

$$FRO_2 + HO_2 \rightarrow CF_3CH(OH)C(O)F \quad (R3)$$

The rate constants for reactions R2 and R3 are based on IUPAC recommendations for similar species (Ammann et al., 2016). The hydroxy-carbonyl product (R3) is removed from the atmosphere by reacting with hydroxyl radical forming 3,3,3-trifluoro-2-oxo-propionyl fluoride, $CF_3C(O)C(O)F$, and CF_3CHO:

$$CF_3CH(OH)C(O)F + OH \rightarrow CF_3C(O)C(O)F + HO_2 \quad (R4a)$$

$$CF_3CH(OH)C(O)F + OH \rightarrow CF_3CHO + FCO_3 \quad (R4b)$$

We included the photolysis of $CF_3C(O)C(O)F$, which forms acyl peroxy radicals ($CF_3C(O)O_2$) given as:

$$CF_3C(O)C(O)F + h\nu \rightarrow CF_3C(O)O_2 \quad (R4c)$$

A wavelength dependent cross-section of $CH_3C(O)CHO$ (Ammann et al., 2016) was used for $CF_3C(O)C(O)F$ as shown in Fig. S1 of the Supplement. The wavelength dependent quantum yield is also based on $CH_3C(O)CHO$ and is 1 between 225-380 nm but decreases at higher wavelengths.

There are two major pathways for the degradation of CF_3CHO in the atmosphere. First, it undergoes photolysis. The initial products formed via photolysis undergo a series of additional reactions to give CO_2 and hydrogen fluoride (HF) (Andersen et al., 2018):

$$CF_3CHO + h\nu \rightarrow CO_2 + HF \quad (R5a)$$

For reaction R5a, we applied a wavelength-dependent cross-section (Ammann et al., 2016), shown in Fig. S1 in the Supplement. A wavelength-dependent quantum yield was calculated considering the recommended values from IUPAC (Ammann et al., 2016) and values from Andersen et al. (Andersen and Nielsen, 2022). Second, oxidation initiated by OH radical produces $CF_3C(O)O_2$, which can react with HO_2, NO, and NO_2.

$$CF_3CHO + OH \rightarrow CF_3C(O)O_2 \quad (R5b)$$

Because IUPAC only provides a rate recommendation for R5b at 298 K (Ammann et al., 2016), we determined the temperature dependence of R5b using IUPAC recommendations for CCl_3CHO, which has comparable reactivity. There are several reactions and reaction channels for $CF_3C(O)O_2$ that compete with its TFA-forming reaction with HO_2:

$$CF_3C(O)O_2 + NO \rightarrow CF_3C(O)O + NO_2 \quad (R6a)$$

https://doi.org/10.5194/egusphere-2025-1031
Preprint. Discussion started: 23 April 2025

$$CF_3C(O)O_2 + NO_2\,(+M) \rightarrow CF_3C(O)OONO_2\,(+M) \quad \text{(R6b)}$$

$$CF_3C(O)OONO_2 \rightarrow CF_3C(O)O_2 + NO_2 \quad \text{(R6c)}$$

$$CF_3C(O)O_2 + HO_2 \rightarrow CF_3C(O)OOH \quad \text{(R7a)}$$

$$CF_3C(O)O_2 + HO_2 \rightarrow CF_3C(O)OH + O_3 \quad \text{(R7b)}$$

$$CF_3C(O)O_2 + HO_2 \rightarrow CF_3C(O)O + O_2 + OH \quad \text{(R7c)}$$

According to kinetic analysis data from Maricq et al. (Maricq et al., 1996) and Wallington et al. (Wallington et al., 1994), IUPAC recommends a rate constant for reaction R6a of 4.02×10^{-12} exp(560/T) cm^3 $molecule^{-1}$ s^{-1}. Reaction R6b is a termolecular reaction, with its rate coefficient depending on pressure. The IUPAC recommended value for this rate coefficient is based on data from Wallington et al. (Wallington et al., 1994). The product of reaction R6b is trifluoracetyl peroxy nitrate (TFPAN), which is thermally unstable and dissociates back into reactants (reaction R6c) at higher temperatures, exhibiting strong temperature dependence. The TFPAN lifetime ranges from approximately 0.5 days at the Earth's surface to several months or even years at higher altitudes (Ammann et al., 2016). Consequently, TFPAN is expected to undergo significant transport within the troposphere and can serve as a reservoir for $CF_3C(O)O_2$, which may be released again in warmer regions. In addition to R6c, TFPAN can also photolyze:

$$CF_3C(O)OONO_2 + h\nu \rightarrow 0.5CF_3C(O)O_2 + 0.5NO_2 + 0.5CF_3C(O)O + 0.5NO_3$$

The assigned photolysis rates for TFPAN are based on the absorption cross sections recommended by the NASA JPL (Burkholder et al., 2020), and typically result in a lifetime with respect to photolysis of about 2 or 3 weeks, with photolysis becoming the major loss reaction at altitudes above about 4 km. Reactions R7a-R7c comprise a complex sequence of processes, with reaction R7b forming TFA ($CF_3C(O)OH$). Because the branching ratios for R7a-c have been evaluated at only 296 K by (Sulbaek Andersen et al., 2004), we have considered them to be temperature independent in this study. Among these reactions, R7c is predominant with a branching ratio of 0.56 ± 0.05, followed by R7b with 0.38 ± 0.04 and R7a with 0.09 ± 0.04. By analogy with the corresponding reaction for $CH_3C(O)O_2$, the contribution of channel (R7a) might be expected to increase at lower temperatures and needs to be experimentally investigated. We have also considered the reaction of $CF_3C(O)O_2$ with the tropospheric pool of peroxy radicals, RO_2, i.e., CH_3O_2. The reaction in this case was based on the IUPAC recommendation for the reaction of $CH_3C(O)O_2$ with CH_3O_2:

$$CF_3C(O)O_2 + CH_3O_2 \rightarrow CF_3C(O)O \quad \text{(R8a)}$$

$$CF_3C(O)O_2 + CH_3O_2 \rightarrow CF_3C(O)OH \quad \text{(R8b)}$$

Reaction R8b provides an additional pathway to TFA formation but is calculated to be an order of magnitude less important than reaction R7b. CF_3CHO formed in reaction R4b can react with HO_2 (reaction R5c) that has been characterized in a theoretical study by Long et al. (Long et al., 2022).

https://doi.org/10.5194/egusphere-2025-1031
Preprint. Discussion started: 23 April 2025

$$CF_3CHO + HO_2 \rightarrow CF_3CH(OH)O_2 \quad \text{(R5c)}$$

Under most tropospheric conditions, the significance of reaction R5c is constrained by the rapid thermal decomposition of the peroxy radical, $CF_3CH(OH)O_2$, which produces CF_3CHO and HO_2 (reaction R9a), as reported by Long et al. (Long et al., 2022). However, this decomposition rate is highly temperature dependent. At the lower temperatures found in the upper troposphere, the subsequent reactions of $CF_3CH(OH)O_2$ with NO (reaction R9b) and HO_2 (reaction R9c) become competitive, potentially creating pathways for TFA formation. Reaction R9b combines two potential pathways for the initially formed intermediate species $CF_3CH(OH)O$, which can decompose to form HCOOH (Orlando et al., 2000; Jenkin et al., 2005) and $CF_3C(O)O$ or can react with O_2 to form TFA and HO_2. While the decomposition pathway is expected to be significant throughout the troposphere, reaction with O_2 may be competitive at high altitudes and low temperatures and its inclusion in the chemical mechanism likely provides an upper estimate of TFA formation.

$$CF_3CH(OH)O_2 \rightarrow CF_3CHO + HO_2 \quad \text{(R9a)}$$

$$CF_3CH(OH)O_2 + NO \rightarrow 0.5HCOOH + 0.5CF_3C(O)O + 0.5CF_3C(O)OH + 0.5HO_2 + NO_2 \quad \text{(R9b)}$$

$$CF_3CH(OH)O_2 + HO_2 \rightarrow 0.5CF_3CH(OH)OOH + 0.5CF_3C(O)OH + 0.2OH + 0.2HO_2 \quad \text{(R9c)}$$

The impact of reactions R9a, R9b, and R9c on TFA formation is critically dependent on the competition between the thermal decomposition of the peroxy radical (R9a) and its reaction with NO (R9b) and HO_2 (R9c). Additionally, $CF_3CH(OH)OOH$ can be oxidized by the OH radical and can also undergo photolysis, and reactions R10a and R10c have the potential to lead to TFA formation.

$$CF_3CH(OH)OOH + OH \rightarrow CF_3C(O)OH + OH \quad \text{(R10a)}$$

$$CF_3CH(OH)OOH + OH \rightarrow CF_3CH(OH)O_2 \quad \text{(R10b)}$$

$$CF_3CH(OH)OOH + h\nu \rightarrow 0.5CF_3C(O)O + 0.5HCOOH + 0.5CF_3C(O)OH + 0.5HO_2 + OH \quad \text{(R10c)}$$

A wavelength dependent cross-section for CH_3OOH was applied to $CF_3CH(OH)OOH$ in reaction R10c as recommended by IUPAC (Fig. S1 in the Supplement). Gas-phase TFA is expected to be deposited either through dry or wet deposition or by reacting with OH radicals as follows:

$$CF_3C(O)OH + OH \rightarrow CF_3C(O)O \quad \text{(R11)}$$

2.4 Surface fate and transport modelling of TFA

We next performed modeling to assess the fate and transport of TFA in the surface water resulting from environmental TFA deposition due to atmospheric degradation of HFO-1234ze(E) via reactions presented in Section 2.3. To this end, we chose the Hudson River, Rhine River, and the Cauvery River as they represent prominent watersheds in the northeast United States

https://doi.org/10.5194/egusphere-2025-1031
Preprint. Discussion started: 23 April 2025

(U.S.), northern Europe, and southern India, respectively, with relatively large populations (see Fig. S9-S11 in the Supplement). The TFA concentrations in the surface water, sediment, and soil in the Hudson River, Rhine River, and Cauvery River watersheds were simulated through fate and transport modeling based on the model-predicted annual average deposition rates (see Results & Discussion). The modeling methodology aligns with the USEPA Human Health Risk Assessment Protocol (HHRAP) for Hazardous Waste Combustion Facilities (Epa, 2005). We determined the TFA loading of the water column using the following mechanisms: *1*) Direct deposition, *2*) Runoff from surfaces within the watershed, *3*) Soil erosion over the total watershed, *4*) Benthic burial, *5*) Inputs from the upstream river segment, and *6*) Discharge to ocean. We assumed that the contributions from other potential mechanisms as compared to those listed above are negligible. Because TFA is resistant to degradation in the environment, we do not account for chemical or biological transformation of TFA after it is deposited on the ground or on surface water. In this model, we have not considered evaporative loss of TFA into the environment because TFA ionizes in water and should not evaporate in the river. Table 1 lists the physical and chemical properties of TFA used in the modeling.

Table 1. Physical/Chemical Properties for TFA

Parameter	Value
Organic Carbon-Water Partition Coefficient[1]	6.22 L/kg
Soil-Water Partition Coefficient[2]	0.94 L/kg
Soil Enrichment Ratio[3]	3
Suspended Sediment/Surface Water Partition Coefficient[4]	0.47 L/kg
Bed Sediment/Sediment Pore Water Partition Coefficient[5]	0.25 L/kg
Diffusivity in Water*	8.00×10^{-6} cm^2/s

[1] calculated according to the equation from Sabljic and Güsten (Güsten and Sabljic, 1995)), using the class of non-hydrophobic chemicals. In the case of TFA, the class "organic acid" is more relevant. Therefore the Koc is calculated as follows: logKoc = 0.6 * logKow + 0.32, with LogKow = 0.79 (ECHA TFA Endpoint Summary for Transport and Distribution - Adsorption/Desorption: https://echa.europa.eu/registration-dossier/-/registered-dossier/5203/5/5/2). [2] Adsortion/desorption tests results show that TFA is poorly adsorbed to the soil and is considered as a mobile organic compound in the majority of soils investigated. The Kd ranged between 0.17 to 20 L/kg for organic and mineral soils (the organic horizon exhibiting greater retention) giving a geometric mean of 0.94 L/kg (SD=4.86, n= 20) (ECHA TFA Endpoint Summary for Transport and Distribution - Adsorption/Desorption: https://echa.europa.eu/registration-dossier/-/registered-dossier/5203/5/5/2). [3] Default value for organic compounds ((Epa, 2005), Appendix B, Table B-4-11)
[4] Calculated using the Koc and a default mid-range value of surface water foc of 0.075 ((Epa, 2005), Appendix A-2). [5] Calculated using the Koc and a default mid-range value of sediment foc of 0.04 ((Epa, 2005), Appendix A-2). * Taken from George et al. (George et al., 1994). Notes: cm^2/s: Square centimetre per second; foc: Fraction of organic carbon; L/kg: Liter per kilogram; Koc: Organic Carbon-Water Partition Coefficient

To simulate mobilization of TFA in watershed sub-basins, we used a series of compartment models that represent the sub-basins in a river system from the headwaters to the mouth of the river where it discharges into the ocean (Figure 2). Note that for Hudson watershed, we did not evaluate the lower Hudson River sub-basin because this section of the Hudson is generally the zone of greatest mixing of river water and the Atlantic Ocean.

Our surface fate and transport model predicts the steady-state concentrations of TFA in the water column and sediment layer beneath the water column. It does not account for the fluctuating flow of TFA between the water column and sediment in response to variations in external inputs. The overall concentration of TFA is divided between the sediment and the water column. Per HHRAP Guidance, the rate of soil erosion from the watershed is calculated by the Universal Soil Loss Equation (USLE) and a sediment delivery ratio. The sum of the TFA concentration dissolved in water and the TFA concentration

https://doi.org/10.5194/egusphere-2025-1031
Preprint. Discussion started: 23 April 2025

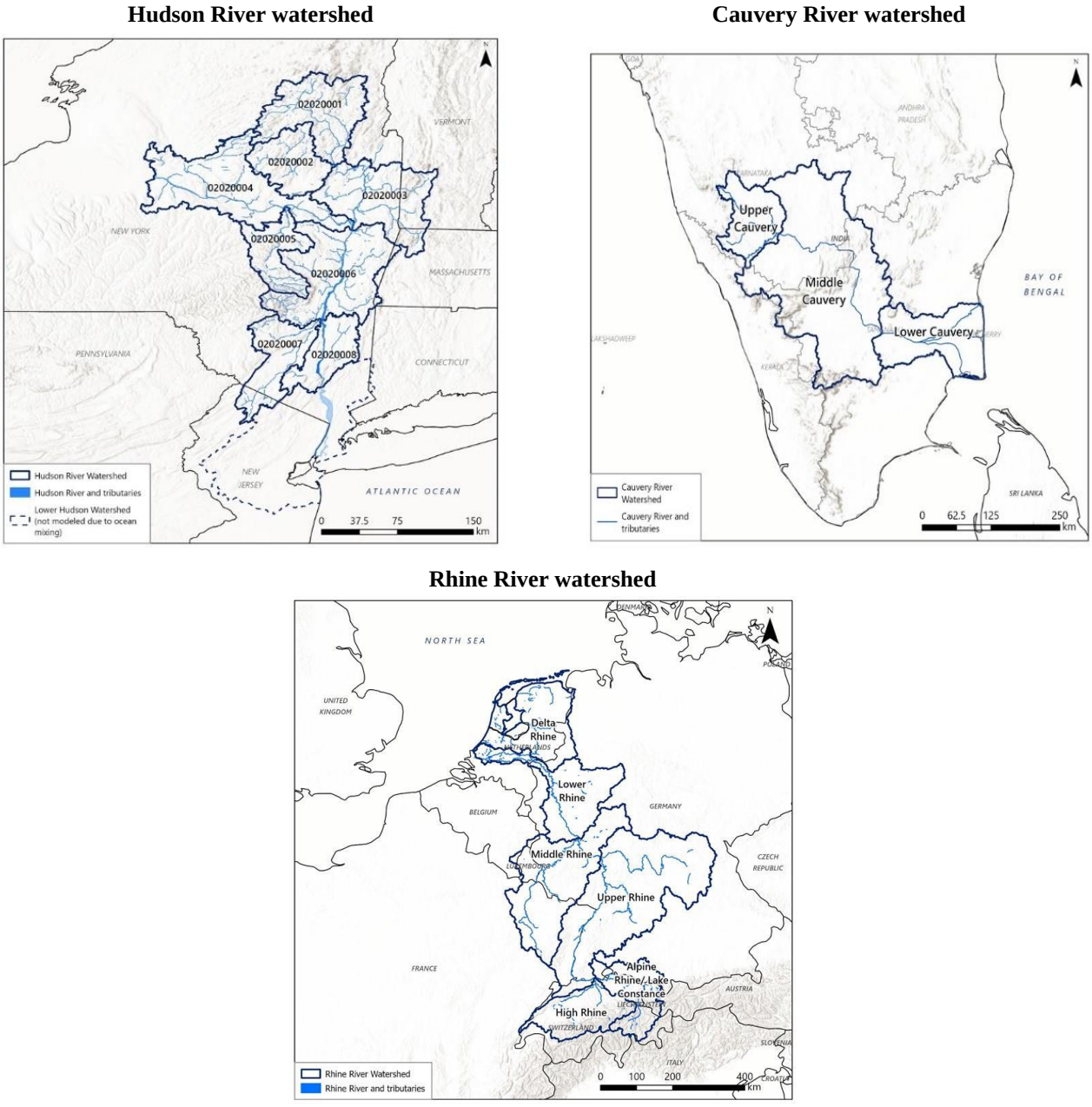

Figure 2. Sub-Basins in the Hudson River watershed (upper-left), Cauvery River watershed (upper-right), and Rhine River watershed (bottom). Note that we modelled the Hudson River watershed assuming the following three sub-basins: Sub-basin #1: 02020001 and 02020002; Sub-basin #2: 02020003, 02020004 and 02020005; and Sub-basin #3: 02020006, 02020007 and 02020008. The lower Hudson River sub-watershed was not evaluated because this zone has high mixing of river water and the Atlantic Ocean.

associated with suspended solids constitutes the total estimated water column TFA concentration. The detailed methodology and governing equations used in the modelling are outlined in the USEPA HHRAP Guidance (Epa, 2005). In the Supplement

https://doi.org/10.5194/egusphere-2025-1031
Preprint. Discussion started: 23 April 2025

(Tables S2-S7), we have summarized the watershed and waterbody parameters for each sub-basin for the Hudson River, Rhine River, and Cauvery River. Some default modeling parameters are available, and these recommended values typically reflect national average conditions in the United States, such as the default empirical intercept coefficient of 0.6 for watersheds larger than 1000 square miles or 2560 square kilometers from the USEPA HHRAP (Epa, 2005) which was used in the modeling for all three rivers. The uncertainties associated with the selection of the watershed and waterbody parameters are also discussed in Section S1 of the Supplement.

3. Results and Discussion

3.1 Global HFO-1234ze(E) emissions and TFA deposition flux

We used monthly pMDI sales data from top 51 countries to calculate the total NGP emissions per month per country, assuming daily dose of 4 puffs/day and ~14 g of HFO-1234ze(E) per pMDI. The spatial distribution of HFO-1234ze(E) emissions within each country in the GEOS-Chem model was estimated using anthropogenic nitric oxide (NO) emissions from the CEDS inventory as a proxy, based on the assumption that NO emissions from residential and commercial sectors correlate with population density and, hence, pMDI usage. Figure 3 shows the annual spatial distribution of HFO-1234ze(E) emissions at a 2°×2.5° resolution in GEOS-Chem, and Table 2 provides the HFO-1234ze(E) emissions in different regions of the world and the entire world. The worldwide emissions of HFO-1234ze(E) from pMDI use in the 51 countries are estimated to be 4.736 Gg/yr (or kilotons/year). Although respiratory disease symptoms can vary by season, our estimates of HFO-1234ze(E) emissions show small variations with different seasons suggesting sustained demand of pMDIs in the respiratory disease community (Fig. S2 in the Supplement).

Table 2. Estimated HFO-1234ze(E) emission flux

Regions	HFO-1234ze(E) emissions
United States	2.38×10^{-5} kg/m^2-yr
Europe	4.26×10^{-5} kg/m^2-yr
Asia	1.58×10^{-5} kg/m^2-yr
South America	0.799×10^{-5} kg/m^2-yr
Rest of the world	1.21×10^{-5} kg/m^2-yr
Global emissions flux	4.736×10^{6} kg/yr

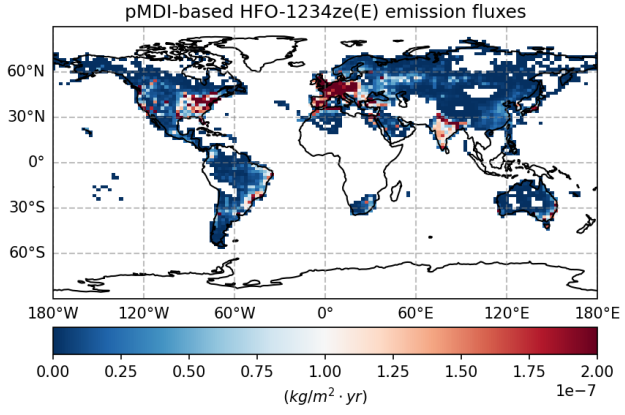

Figure 3: Global annual distribution of HFO-1234ze(E) emissions at 2°×2.5° resolution in GEOS-Chem. This distribution of HFO-1234ze(E) emissions is based on global pMDI sales data, assuming all pMDI devices sold in 2022 used HFO-1234ze(E) as the propellant.

We followed the formulation of Wesely (Wesely, 2007), subsequently modified by Wang et al. (Wang et al., 1998), for computation of dry deposition of gas-phase species onto surfaces in GEOS-Chem, which calculates dry deposition velocities

https://doi.org/10.5194/egusphere-2025-1031
Preprint. Discussion started: 23 April 2025

using data for surface momentum, sensible heat fluxes, temperature, and solar radiation. To incorporate the dry deposition of TFA, we assumed its behaviour in this process to be analogous to that of nitric acid, following the approach of Luecken et al. (Luecken et al., 2010) and Henne et al. (Henne et al., 2012). Figure 4 shows the modelled annual global dry and wet deposition fluxes of TFA. Interestingly, these annual dry and wet TFA deposition fluxes are akin to another three-dimensional model study (Andersen et al., 2018) that investigated a different hydrofluoroolefin, HFO-1233zd(E), which is structurally similar to HFO-1234ze(E), suggesting atmospheric degradation mechanisms of both these chemicals are similar. The monthly variations in global dry and wet deposition of TFA are shown in Figs. S3–S4 in the Supplement, which capture the effect of different seasons on TFA deposition fluxes globally. We found that the total deposition between 0° and 45° north latitudes is approximately 61% of the global total deposition. Even though NGP emission fluxes are four times lower in Africa as compared to Europe (Table 2), the dry deposition fluxes are higher in Africa as compared to Europe. This is largely due to the higher concentration of hydroxyl radicals around the equator (Pimlott et al., 2022) that will increase the formation of $CF_3CO(O)_2$ from TFAA via reaction 5b (R5b).

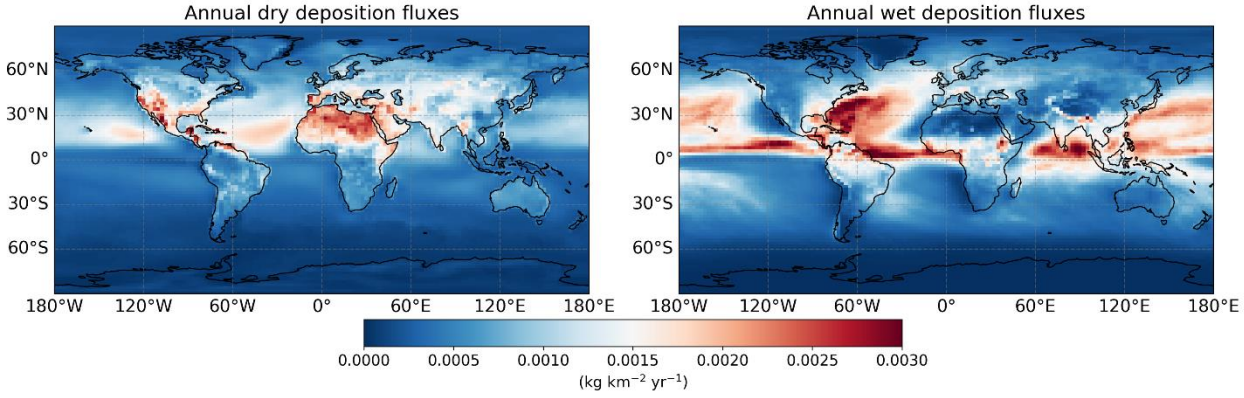

Figure 4: Annual global dry and wet deposition fluxes of TFA. These fluxes reflect the average of TFA deposited over a year. Note that dry deposition fluxes are highest in African region and wet deposition fluxes are highest around the ocean near the northern tropical region

To understand the effects of seasonal variation and altitude on TFA-deposition fluxes in two identified regions in Europe and Africa (Fig. S5 in the Supplement), we computed correlation between daily TFAA and TFA formed per day for each month at different altitudes (Fig. S6 in the Supplement). We found a negative correlation between TFAA and TFA in the identified regions of Europe and Africa for almost the entire year, confirming that the hydroxyl radical channel (R5b) is the primary route of TFA formation under different environmental conditions. In contrast to this general agreement, we found that reaction channels other than R5b contribute to TFA formation during May thru September in the identified region of Africa (Fig. S6 in the Supplement; $\rho \approx 0$).

https://doi.org/10.5194/egusphere-2025-1031
Preprint. Discussion started: 23 April 2025

To understand contribution of primary TFA-forming pathways on the spatial pattern of TFA, we examined concentrations of various-related species at the surface after the last spin-up simulations at 4°×5° resolution (see Methods). Our assessment of initial oxidation products suggests that HFO-1234ze(E) emissions at the surface largely correlate with corresponding TFAA concentrations at the surface (Fig. S7 in the Supplement) and show little correspondence with the initial oxidation products. The subsequent degradation of TFAA can occur via OH (reaction R5b) or HO_2 (reaction R5c); of these two possible routes, the OH-pathway which forms $CF3C(O)O_2$ is about three orders of magnitude faster as compared to the HO_2 pathway (Table S1), leading to more $CF_3C(O)O_2$ concentrations (R5b) than $CF_3CH(OH)O_2$ (R5c), see Fig. S8 in the Supplement. Lastly, we calculated the ratio $[HO_2]\times[CF_3C(O)O_2]/[OH]$ to quantify the contribution of species that form TFA (R7b) and that remove TFA from the atmosphere (R11). Figure 5 compares the gas-phase concentrations of TFA and $[HO_2]\times[CF_3C(O)O_2]/[OH]$ at the surface. This analysis suggests that *1*) reactions that form TFA generally dominate over those that remove it in the atmosphere, and *2*) $CF_3C(O)O_2$ reaction is the primary precursor that forms TFA in the atmosphere.

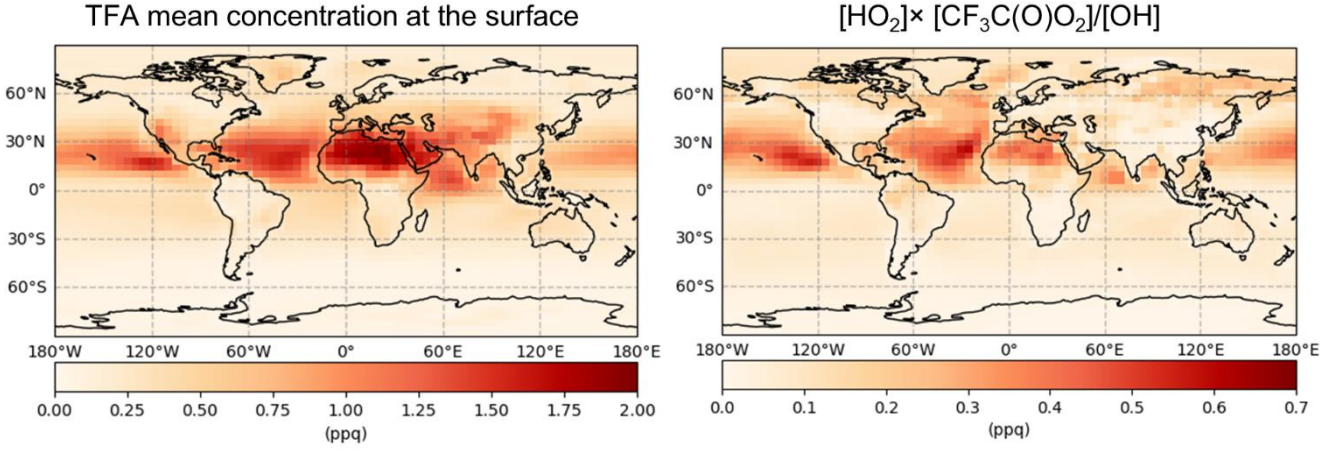

Figure 5: Annual mean-surface concentrations (gas-phase) of TFA and ($[HO_2] \times [CF_3C(O)O_2]$)/[OH] at 4°×5° resolution. The spatial pattern of the ratio of ($[HO_2]$ x $[CF_3C(O)O_2]$)/[OH] generally matches the spatial pattern of the TFA.

3.2 Fate and transport modelling of pMDI-derived TFA

This section presents and discusses the modelled TFA concentrations in the surface water, surface sediment, and surface soil for the sub-basins of each of the three river watersheds and the mass balance of TFA in these systems. We have used the methodology described in Section 2.4 for estimating the TFA concentrations in the sub-basins of the Hudson, Rhine, and Cauvery River watersheds. The model is based on a series of connected compartment models for each sub-basin of the river system. The input of TFA from atmospheric deposition into the compartment for a sub-basin is based on area-weighted average (calculated based on the % of the grid cell areas overlapping with the sub-basin) TFA deposition flux for that sub-basin. Figure 6 shows the grid cells encasing spatial distribution of the total (dry + wet) TFA deposition flux and Table 3 lists weighted-average TFA deposition flux for each sub-basin of the three watersheds. Note that the distinct colour scales in Figure 6 capture differences in the total TFA deposition flux values in the three watersheds.

https://doi.org/10.5194/egusphere-2025-1031
Preprint. Discussion started: 23 April 2025

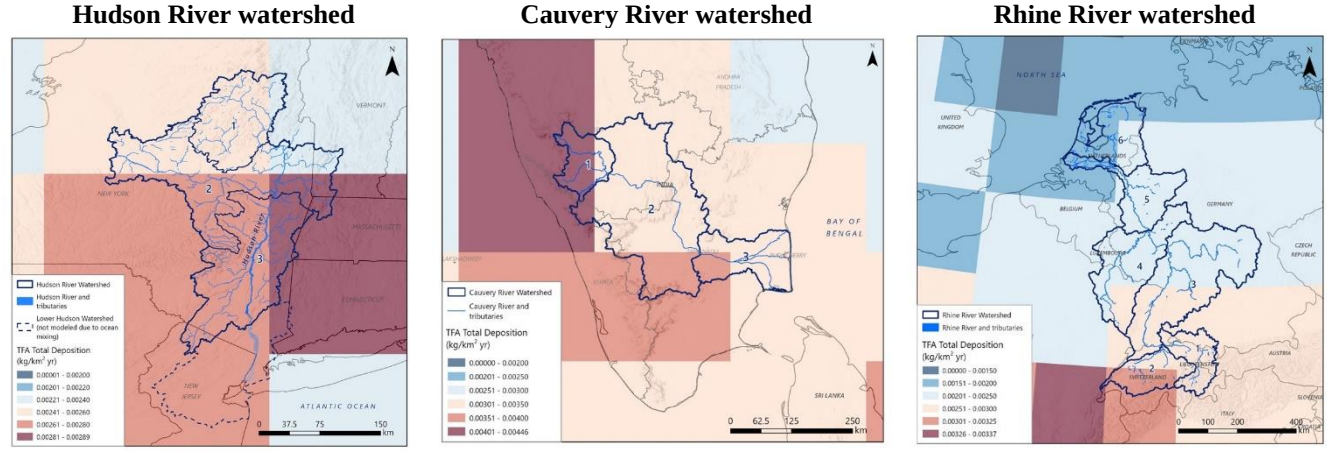

Figure 6. Estimated total TFA gridded deposition in the Hudson River watershed and surrounding area, in the Cauvery River watershed and surrounding area, and in the Rhine River watershed and surrounding area. Note that the color scale changes for each figure to display the range of deposition values within the extent of the map. *Cauvery watershed*: Sub-basin 1, Upper Cauvery; Sub-basin 2, Middle Cauvery; Sub-basin 3, Lower Cauvery. *Rhine watershed*: Sub-basin 1, Alpine Rhine; 2, High Rhine; 3, Upper Rhine; 4, Middle Rhine; 5, Lower Rhine; and 6, Delta Rhine. Hudson sub-basins are as described in the Method section.

Assuming the annual TFA deposition fluxes (Table 3) do not change over time, we estimated net TFA accumulations in the surface water, soil, and sediment of the three watersheds for a period of 30 years. Based on the simulation results, the TFA concentrations in various river systems reach a steady state at different rates (Figure 7), influenced by factors such as volumetric flow rates and deposition rates across sub-basins. We found that TFA concentrations reached steady state within one year in the Hudson River. Model predicted peak surface water TFA concentrations range from 2 ng/L in the upstream sub-basin (sub-basin 1) to 5.4 ng/L in the middle sub-basin (sub-basin 2). We found that these TFA accumulation variations within the sub-basins are impacted by factors such as differences in River flow rates, infiltration rates of the watersheds (see Tables S2-S7 in the Supplement), and deposition rates (Table 3). Based on the simulation results of the TFA mass allocation in soil, sediment, surface water in the river, and the ocean, approximately 63% of the TFA mass deposited from the air would be delivered to the ocean.

Table 3. Annual Average Atmospheric Deposition Flux of TFA (μg/m^2-yr)

Sub-Basin	Dry Deposition	Wet Deposition	Total Deposition
Hudson River watershed			
1	1.314	1.159	2.472
2	1.371	1.237	2.608
3	1.430	1.321	2.751
Cauvery River watershed			
1	1.520	2.618	4.138
2	1.637	1.879	3.515
3	1.414	1.857	3.271
Rhine River watershed			
1	1.207	1.539	2.746
2	1.308	1.618	2.926
3	1.354	1.104	2.459
4	1.293	1.035	2.328
5	1.152	0.967	2.119
6	0.956	1.002	1.958

Akin to the Hudson River results, we found that peak TFA surface water concentrations in Cauvery sub-basins also reached steady state within a year. The model-predicted TFA concentrations range from 8.9 ng/L in the upper Cauvery sub-basin to 19.3 ng/L in the middle Cauvery sub-basin. Based on our TFA mass-allocation calculations, roughly 19% of the TFA mass

https://doi.org/10.5194/egusphere-2025-1031
Preprint. Discussion started: 23 April 2025

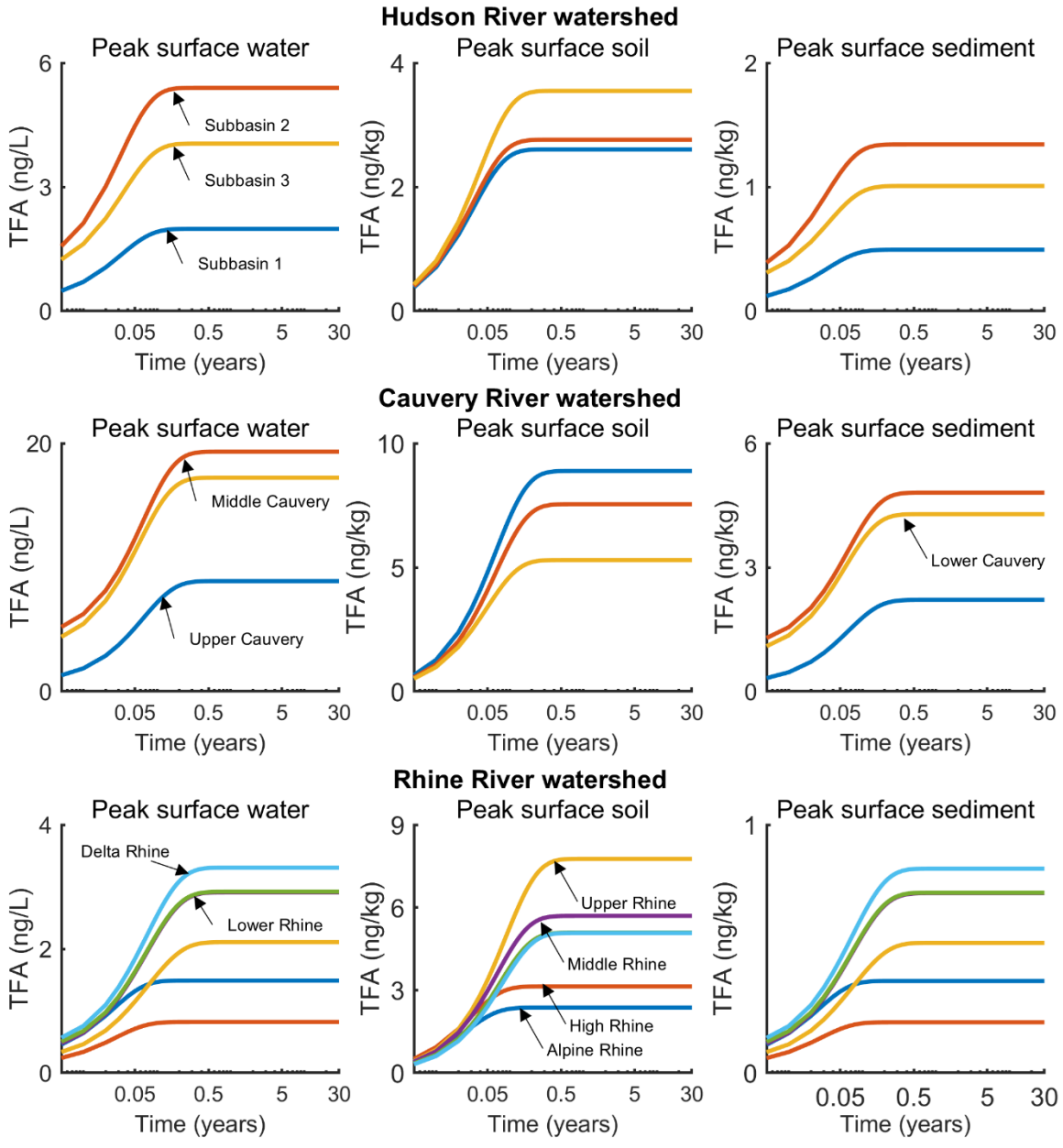

Figure 7: Model predicted concentrations of TFA in surface water, surface soil, and surface sediment of Hudson River watershed (first row), Cauvery River watershed (middle row), and Rhine River watershed (bottom row) due to 30-years of continued NGP emissions via pMDI sales/usage.

360 deposited from the air would be transported to the ocean, a small percentage (~4%) would remain in the river system (i.e., surface water and surface sediment) or the mixing zone of surface soil receiving deposition (i.e., assumed to be the top 2 centimeters of soil for this study), and roughly four-fifths would leach to deep soil or sediment, after the TFA concentrations

https://doi.org/10.5194/egusphere-2025-1031
Preprint. Discussion started: 23 April 2025

reach steady state in the system (Figure 7). The TFA mass allocation percentage to deep soil is higher for the Cauvery River basin than that for Hudson River basin and Rhine River basin (next paragraph) because Cauvery River is located in the tropical/sub-tropical zone and has much higher precipitation rates, and therefore, higher infiltration rates (determined by precipitation, irrigation, run-off, and evapotranspiration in the basin) which caused increased leaching process of TFA to deep soil in this basin.

Akin to the other two watersheds, the peak surface water concentrations of TFA in the Rhine River sub-basins also reached steady state within a year, suggesting that region-specific TFA deposition differences are unsubstantial compared to River-specific flow rates' impact on the time of TFA to reach steady state in the river system. The peak surface water TFA concentrations in the three watersheds all reach steady state relatively quickly within the first year with some small variations, mainly due to the different flow rates relative to the water volumes in the rivers. The model-predicted surface water TFA concentrations range from 0.8 ng/L in High Rhine sub-basin to 3.3 ng/L in the Delta Rhine sub-basin. The Alphine Rhine sub-basin has higher peak concentrations than High Rhine sub-basin due to lower flow rates and higher suspended solids. Based on our TFA mass-allocation calculations, approximately 63% of the TFA mass deposited from the air into the ocean, after the TFA concentrations reached steady state in the surface water and surface soil. According to Sturm et al. (Sturm et al., 2023), measurements of TFA in the surface water of the Rhine River are 400 ng/L near Karlsruhe, Germany (in the Upper Rhine, sub-basin 3) and 1,100 ng/L near Mainz, Germany (in the Middle Rhine, sub-basin 4). These measurements suggest that future pMDIs using NGP as the medical propellant will form negligible TFA (up to 3.3 ng/L, equivalent to less than 1% of total) in Rhine surface water as compared to other sources that form TFA in the Rhine surface water.

4. Conclusions

Inhaled respiratory medications delivered by pMDIs are relied upon by millions of patients, accounting for 78% of inhaler usage globally (Bell et al., 2023). Due to their high GWP, present-day medical propellants (HFCs) are subject to phase down, under the Kigali amendment. In this study, we estimated environmental TFA accumulation due to prospective usage of pMDIs that have HFO-1234ze(E), as the medical propellant which is not subject to phase-down under the Kigali amendment due to its low GWP. In this study, we investigated atmospheric and surface behavior of HFO-1234ze(E) and its atmospheric breakdown product TFA, focusing on deposition and transport of TFA within the Hudson, Rhine, and Cauvery River watersheds due to continued usage of these prospective pMDIs.

Based on annual pMDI sales data of all manufacturers from the top fifty-one countries, we estimate global NGP emissions to be around 4.736 Gg/year, concentrated in densely populated regions. Using the GEOS-Chem atmospheric model, adapted for MCM of HFO-1234ze(E), we simulated the effect of prospective pMDI usage, i.e., HFO-1234ze(E) emissions, on environmental TFA deposition patterns. Next, watershed-specific models that follow USEPA guidelines were used to estimate TFA concentrations over 30 years, showcasing how atmospheric TFA may spreads from rivers into the ocean

https://doi.org/10.5194/egusphere-2025-1031
Preprint. Discussion started: 23 April 2025

following due to continued pMDI usage. Our study reveals that atmospheric TFA may deposit in soil and water bodies remote to pMDI usage, owing to its mobility and solubility.

Atmospheric and watershed modeling predicts that future pMDI usage would lead to TFA concentrations in surface waters between 0.8 to 19.3 ng/L, surface soil between 2.3 to 8.8 ng/kg, and surface sediment between 0.2 to 4.8 ng/kg across the three studied watersheds. These differences in TFA concentrations are due to local variables such as volumetric flow rates and region-specific TFA deposition rates, i.e., pMDI usage and weather conditions. To put things in perspective,

i) Consider German EPA's precautionary threshold of TFA in drinking water, i.e., 10,000 ng/L (Arp et al., 2024), which suggests that margin-of-exposure for pMDI associated TFA in drinking water is greater than 500;

ii) Consider REACH dossier's long-term no-observed effect concentration (NOEC) of soil TFA, i.e., 830,000 ng/kg (Arp et al., 2024), which suggests that TFA soil accumulation due NGP emissions via prospective pMDI usage are greater than 90,000-fold below the concentrations known to affect plant-shoot growth (Arp et al., 2024); and

iii) Considering lowest reported concentration of TFA in Rhine surface water, i.e., 400 ng/L (Sturm et al., 2023), these result suggest that prospective NGP emissions via pMDI usage would form less than 1% of the TFA in Rhine surface water; in other words, 99% of Rhine surface water can be attributed to other sources of environmental TFA.

Together, these results demonstrate that even if HFO-1234ze(E) was the sole medical propellant of future pMDIs, its continuous emission in the atmosphere would form negligible quantities of surface water and surface soil TFA, i.e., in concentrations that are several orders of magnitude below the concentrations of TFA that may cause human and/or crop toxicity. These findings, coupled with its near-zero GWP, reinforce the importance of HFO-1234ze(E) as a viable, long-term alternative to existing medical propellants.

Code/Data availability

The original contributions presented in the study are included in the article and the supplement. Additional data and information are available from the corresponding author upon reasonable request.

Author contribution

SGT designed the study and prepared the draft. SGT, KV, KZ, LMD, KT, FK, YZ, BY, and CH performed the data analysis. All authors edited the manuscript.

https://doi.org/10.5194/egusphere-2025-1031
Preprint. Discussion started: 23 April 2025

Competing interests

SGT, PG, HK, MG, and SP are employees of AstraZeneca and hold shares/share options in AstraZeneca. KV, KZ, LMD, KT, FK, YZ, and BY are employees of Ramboll. DKP is an employee of Honeywell.

Acknowledgements

The authors thank Michael E. Jenkin for developing the Master Chemical Mechanism of HFO-1234ze(E) and preparing the artwork illustrating its atmospheric degradation pathways; Zongrun Li and Viral Shah for their valuable assistance in incorporating photolysis reactions in GEOS-Chem; and Nigel Budgen for providing the global monthly pMDI sales data that were used for estimating world-wide HFO-1234ze(E) emissions.

References

Adlunger, K., Anke, J., Bachem, G., Banning, H., Biegel-Engler, A., Blondzik, K., Braun, U., Eckhardt, A., Gildemeister, D., Hilliges, F., Hoffmann, G., Jentzsch, F., Klitzke, S., Kuckelkorn, J., Martens, K., Müller, A., Pickl, C., Pirntke, U., Rechenberg, J., Sättler, D., Schmidt, U., Speichert, G., Warnke, I., Wehner, J., and Wischer, R.: Reducing the input of chemicals into waters: trifluoroacetate (TFA) as a persistent and mobile substance with many sources, 2021.

Ammann, M., Cox, R., Crowley, J., Jenkin, M., Mellouki, A., Rossi, M., Troe, J., Wallington, T., Cox, B., and Atkinson, R.: IUPAC task group on atmospheric chemical kinetic data evaluation, 2016.

Andersen, M. P. S. and Nielsen, O. J.: Tropospheric photolysis of CF3CHO, Atmospheric Environment, 272, 118935, 2022.

Andersen, M. P. S., Schmidt, J. A., Volkova, A., and Wuebbles, D. J.: A three-dimensional model of the atmospheric chemistry of E and Z-CF3CH= CHCl (HCFO-1233 (zd)(E/Z)), Atmospheric Environment, 179, 250-259, 2018.

Arp, H. P. H., Gredelj, A., Glüge, J., Scheringer, M., and Cousins, I. T.: The global threat from the irreversible accumulation of trifluoroacetic acid (TFA), Environmental Science & Technology, 58, 19925-19935, 2024.

Bell, J., Ringall, A., Khezrian, M., Kocks, J., and Usmani, O.: An assessment of pressurized metered-dose inhaler use in countries in Europe and the rest of the world, in: D22. Hot topics in behavioral sciences and health services research, American Thoracic Society, A6315-A6315, 2023.

Bian, H. and Prather, M. J.: Fast-J2: Accurate simulation of stratospheric photolysis in global chemical models, Journal of atmospheric chemistry, 41, 281-296, 2002.

Burkholder, J., Sander, S., Abbatt, J., Barker, J., Cappa, C., Crounse, J., Dibble, T., Huie, R., Kolb, C., and Kurylo, M.: Chemical kinetics and photochemical data for use in atmospheric studies; evaluation number 19, Pasadena, CA: Jet Propulsion Laboratory, National Aeronautics and Space …, 2020.

Burkholder, J., Sander, S., Abbatt, J., Barker, J., Huie, R., Kolb, C., Kurylo, M., Orkin, V., Wilmouth, D., and Wine, P.: Chemical kinetics and photochemical data for use in atmospheric studies: evaluation number 18, Pasadena, CA: Jet Propulsion Laboratory, National Aeronautics and Space …, 2015a.

Burkholder, J. B., Cox, R., and Ravishankara, A.: Atmospheric degradation of ozone depleting substances, their substitutes, and related species, Chemical Reviews, 115, 3704-3759, 2015b.

Carn, S., Yang, K., Prata, A., and Krotkov, N.: Extending the long-term record of volcanic SO2 emissions with the Ozone Mapping and Profiler Suite nadir mapper, Geophysical Research Letters, 42, 925-932, 2015.

Collaborators, G. B. D. C. R. D.: Prevalence and attributable health burden of chronic respiratory diseases, 1990-2017: a systematic analysis for the Global Burden of Disease Study 2017, Lancet Respir Med, 8, 585-596, 10.1016/S2213-2600(20)30105-3, 2020.

Eastham, S. D., Weisenstein, D. K., and Barrett, S. R.: Development and evaluation of the unified tropospheric–stratospheric chemistry extension (UCX) for the global chemistry-transport model GEOS-Chem, Atmospheric Environment, 89, 52-63, 2014.

EPA, U.: Human health risk assessment protocol for hazardous waste combustion facilities, 2005.

https://doi.org/10.5194/egusphere-2025-1031
Preprint. Discussion started: 23 April 2025

Gelaro, R., McCarty, W., Suárez, M. J., Todling, R., Molod, A., Takacs, L., Randles, C. A., Darmenov, A., Bosilovich, M. G., and Reichle, R.: The modern-era retrospective analysis for research and applications, version 2 (MERRA-2), Journal of climate, 30, 5419-5454, 2017.

George, C., Saison, J., Ponche, J., and Mirabel, P.: Kinetics of mass transfer of carbonyl fluoride, trifluoroacetyl fluoride, and trifluoroacetyl chloride at the air/water interface, The Journal of Physical Chemistry, 98, 10857-10862, 1994.

Guenther, A., Jiang, X., Heald, C. L., Sakulyanontvittaya, T., Duhl, T. a., Emmons, L., and Wang, X.: The Model of Emissions of Gases and Aerosols from Nature version 2.1 (MEGAN2. 1): an extended and updated framework for modeling biogenic emissions, Geoscientific Model Development, 5, 1471-1492, 2012.

Güsten, H. and Sabljic, A.: QSARs for soil sorption, Overview of structure-activity relationships for environmental endpints, Part, 1, 1995.

Heath, E. A.: Amendment to the Montreal protocol on substances that deplete the ozone layer (Kigali amendment), International Legal Materials, 56, 193-205, 2017.

Henne, S., Shallcross, D. E., Reimann, S., Xiao, P., Brunner, D., O'Doherty, S., and Buchmann, B.: Future emissions and atmospheric fate of HFC-1234yf from mobile air conditioners in Europe, Environmental science & technology, 46, 1650-1658, 2012.

Hoesly, R. M., Smith, S. J., Feng, L., Klimont, Z., Janssens-Maenhout, G., Pitkanen, T., Seibert, J. J., Vu, L., Andres, R. J., and Bolt, R. M.: Historical (1750–2014) anthropogenic emissions of reactive gases and aerosols from the Community Emissions Data System (CEDS), Geoscientific Model Development, 11, 369-408, 2018.

Hu, L., Millet, D. B., Baasandorj, M., Griffis, T. J., Turner, P., Helmig, D., Curtis, A. J., and Hueber, J.: Isoprene emissions and impacts over an ecological transition region in the US Upper Midwest inferred from tall tower measurements, Journal of Geophysical Research: Atmospheres, 120, 3553-3571, 2015.

Hudman, R., Moore, N., Mebust, A., Martin, R., Russell, A., Valin, L., and Cohen, R.: Steps towards a mechanistic model of global soil nitric oxide emissions: implementation and space based-constraints, Atmospheric Chemistry and Physics, 12, 7779-7795, 2012.

Jaeglé, L., Quinn, P., Bates, T., Alexander, B., and Lin, J.-T.: Global distribution of sea salt aerosols: new constraints from in situ and remote sensing observations, Atmospheric Chemistry and Physics, 11, 3137-3157, 2011.

Javadi, M. S., Søndergaard, R., Nielsen, O. J., Hurley, M., and Wallington, T.: Atmospheric chemistry of trans-CF 3 CH= CHF: products and mechanisms of hydroxyl radical and chlorine atom initiated oxidation, Atmospheric Chemistry and Physics, 8, 3141-3147, 2008.

Jenkin, M., Young, J., and Rickard, A.: The MCM v3. 3.1 degradation scheme for isoprene, Atmospheric Chemistry and Physics, 15, 11433-11459, 2015.

Jenkin, M., Andersen, M. S., Hurley, M., Wallington, T., Taketani, F., and Matsumi, Y.: A kinetics and mechanistic study of the OH and NO 2 initiated oxidation of cyclohexa-1, 3-diene in the gas phase, Physical Chemistry Chemical Physics, 7, 1194-1204, 2005.

Jenkin, M. E., Saunders, S. M., and Pilling, M. J.: The tropospheric degradation of volatile organic compounds: a protocol for mechanism development, Atmospheric Environment, 31, 81-104, 1997.

Jenkin, M. E., Saunders, S. M., Wagner, V., and Pilling, M. J.: Protocol for the development of the Master Chemical Mechanism, MCM v3 (Part B): tropospheric degradation of aromatic volatile organic compounds, Atmospheric Chemistry and Physics, 3, 181-193, 2003.

Jenkin, M. E., Valorso, R., Aumont, B., and Rickard, A. R.: Estimation of rate coefficients and branching ratios for reactions of organic peroxy radicals for use in automated mechanism construction, Atmospheric Chemistry and Physics, 19, 7691-7717, 2019.

Jenkin, M. E., Valorso, R., Aumont, B., Rickard, A. R., and Wallington, T. J.: Estimation of rate coefficients and branching ratios for gas-phase reactions of OH with aliphatic organic compounds for use in automated mechanism construction, Atmospheric Chemistry and Physics, 18, 9297-9328, 2018.

Kwok, E. S. and Atkinson, R.: Estimation of hydroxyl radical reaction rate constants for gas-phase organic compounds using a structure-reactivity relationship: An update, Atmospheric Environment, 29, 1685-1695, 1995.

Lin, H., Long, M. S., Sander, R., Sandu, A., Yantosca, R. M., Estrada, L. A., Shen, L., and Jacob, D. J.: An Adaptive Auto-Reduction Solver for Speeding Up Integration of Chemical Kinetics in Atmospheric Chemistry Models: Implementation and

https://doi.org/10.5194/egusphere-2025-1031
Preprint. Discussion started: 23 April 2025

Evaluation in the Kinetic Pre-Processor (KPP) Version 3.0. 0, Journal of Advances in Modeling Earth Systems, 15, e2022MS003293, 2023.

Lin, H., Jacob, D. J., Lundgren, E. W., Sulprizio, M. P., Keller, C. A., Fritz, T. M., Eastham, S. D., Emmons, L. K., Campbell, P. C., and Baker, B.: Harmonized Emissions Component (HEMCO) 3.0 as a versatile emissions component for atmospheric models: application in the GEOS-Chem, NASA GEOS, WRF-GC, CESM2, NOAA GEFS-Aerosol, and NOAA UFS models, Geoscientific Model Development, 14, 5487-5506, 2021.

Liu, H., Jacob, D. J., Bey, I., and Yantosca, R. M.: Constraints from 210Pb and 7Be on wet deposition and transport in a global three-dimensional chemical tracer model driven by assimilated meteorological fields, Journal of Geophysical Research: Atmospheres, 106, 12109-12128, 2001.

Logan, L.: EPA Proposes Phasedown Program For Climate-Warming HFCs, Inside EPA's Clean Air Report, 32, 11-11, 2021.

Long, B., Xia, Y., and Truhlar, D. G.: Quantitative kinetics of HO2 reactions with aldehydes in the atmosphere: High-order dynamic correlation, anharmonicity, and falloff effects are all important, Journal of the American Chemical Society, 144, 19910-19920, 2022.

Luecken, D. J., Waterland, R. L., Papasavva, S., Taddonio, K. N., Hutzell, W. T., Rugh, J. P., and Andersen, S. O.: Ozone and TFA impacts in North America from degradation of 2, 3, 3, 3-tetrafluoropropene (HFO-1234yf), a potential greenhouse gas replacement, Environmental science & technology, 44, 343-348, 2010.

Mao, J., Jacob, D. J., Evans, M., Olson, J., Ren, X., Brune, W., St Clair, J., Crounse, J., Spencer, K., and Beaver, M.: Chemistry of hydrogen oxide radicals (HO x) in the Arctic troposphere in spring, Atmospheric Chemistry and Physics, 10, 5823-5838, 2010.

Maricq, M. M., Szente, J. J., Khitrov, G. A., and Francisco, J. S.: The CF3C (O) O2 radical. Its UV spectrum, self-reaction kinetics, and reaction with NO, The Journal of Physical Chemistry, 100, 4514-4520, 1996.

Masson-Delmotte, V., P. Zhai, A. Pirani, S.L. Connors, C. Péan, S. Berger, N. Caud, Y. Chen, L. Goldfarb, M.I. Gomis, M. Huang, K. Leitzell, E. Lonnoy, J.B.R. and Matthews, T. K. M., T. Waterfield, O. Yelekçi, R. Yu, and B. Zhou: Climate Change 2021: The Physical Science Basis. Contribution of Working Group I to the Sixth Assessment Report of the Intergovernmental Panel on
Climate Change, 2021.

Meng, J., Martin, R. V., Ginoux, P., Hammer, M., Sulprizio, M. P., Ridley, D. A., and van Donkelaar, A.: Grid-independent High Resolution Dust Emissions (v1. 0) for Chemical Transport Models: Application to GEOS-Chem (version 12.5. 0), Geoscientific Model Development Discussions, 2020, 1-23, 2020.

Murray, L. T., Jacob, D. J., Logan, J. A., Hudman, R. C., and Koshak, W. J.: Optimized regional and interannual variability of lightning in a global chemical transport model constrained by LIS/OTD satellite data, Journal of Geophysical Research: Atmospheres, 117, 2012.

Neale, R. E., Barnes, P. W., Robson, T. M., Neale, P. J., Williamson, C. E., Zepp, R. G., Wilson, S. R., Madronich, S., Andrady, A. L., and Heikkilä, A. M.: Environmental effects of stratospheric ozone depletion, UV radiation, and interactions with climate change: UNEP Environmental Effects Assessment Panel, Update 2020, Photochemical & Photobiological Sciences, 20, 1-67, 2021.

Orlando, J. J., Nozière, B., Tyndall, G. S., Orzechowska, G. E., Paulson, S. E., and Rudich, Y.: Product studies of the OH- and ozone-initiated oxidation of some monoterpenes, Journal of Geophysical Research: Atmospheres, 105, 11561-11572, 2000.

Pérez-Peña, M. P., Fisher, J. A., Hansen, C., and Kable, S. H.: Assessing the atmospheric fate of trifluoroacetaldehyde (CF 3 CHO) and its potential as a new source of fluoroform (HFC-23) using the AtChem2 box model, Environmental Science: Atmospheres, 3, 1767-1777, 2023.

Pimlott, M. A., Pope, R. J., Kerridge, B. J., Latter, B. G., Knappett, D. S., Heard, D. E., Ventress, L. J., Siddans, R., Feng, W., and Chipperfield, M. P.: Investigating the global OH radical distribution using steady-state approximations and satellite data, Atmospheric Chemistry and Physics, 22, 10467-10488, 2022.

Sander, S., Friedl, R., Golden, D., Kurylo, M., Moortgat, G., Wine, P., Ravishankara, A., Kolb, C., Molina, M., and Finlayson-Pitts, B.: Chemical kinetics and photochemical data for use in atmospheric studies evaluation number 15, 2006.

https://doi.org/10.5194/egusphere-2025-1031
Preprint. Discussion started: 23 April 2025

Sander, S., Friedl, R., Golden, D., Kurylo, M., Moortgat, G., Wine, P., Ravishankara, A., Kolb, C., Molina, M., and Finlyason-Pitts, B.: Chemical kinetics and photochemical data for use in atmospheric studies: Evaluation number 15, Pasadena, CA: Jet Propulsion Laboratory, California Institute of Technology2010.

Saunders, S. M., Jenkin, M. E., Derwent, R. G., and Pilling, M. J.: Protocol for the development of the Master Chemical Mechanism, MCM v3 (Part A): tropospheric degradation of non-aromatic volatile organic compounds, Atmospheric Chemistry and Physics, 3, 161-180, 2003.

Simone, N. W., Stettler, M. E., and Barrett, S. R.: Rapid estimation of global civil aviation emissions with uncertainty quantification, Transportation Research Part D: Transport and Environment, 25, 33-41, 2013.

Søndergaard, R., Nielsen, O. J., Hurley, M., Wallington, T., and Singh, R.: Atmospheric chemistry of trans-CF3CHCHF: kinetics of the gas-phase reactions with Cl atoms, OH radicals, and O3, Chemical physics letters, 443, 199-204, 2007.

Sturm, S., Freeling, F., Bauer, F., Vollmer, T., aus der Beek, T., and Karges, U.: Trifluoroacetate (TFA): Laying the foundations for effective mitigation – Spatial analysis of the input pathways into the water cycle, 2023.

Sulbaek Andersen, M., Stenby, C., Nielsen, O., Hurley, M., Ball, J., Wallington, T., Martin, J., Ellis, D., and Mabury, S.: Atmospheric Chemistry of n-C x F2 x+ 1CHO (x= 1, 3, 4): Mechanism of the C x F2 x+ 1C (O) O2+ HO2 Reaction, The Journal of Physical Chemistry A, 108, 6325-6330, 2004.

Tewari, S. G., Bell, J. P., Budgen, N., Platz, S., Gibbs, M., Newham, P., and Kimko, H.: Pressurized metered-dose inhalers using next-generation propellant HFO-1234ze (E) deposit negligible amounts of trifluoracetic acid in the environment, Frontiers in Environmental Science, 11, 1297920, 2023.

Tzompa-Sosa, Z. A., Mahieu, E., Franco, B., Keller, C. A., Turner, A., Helmig, D., Fried, A., Richter, D., Weibring, P., and Walega, J.: Revisiting global fossil fuel and biofuel emissions of ethane, Journal of Geophysical Research: Atmospheres, 122, 2493-2512, 2017.

Van Der Werf, G. R., Randerson, J. T., Giglio, L., Van Leeuwen, T. T., Chen, Y., Rogers, B. M., Mu, M., Van Marle, M. J., Morton, D. C., and Collatz, G. J.: Global fire emissions estimates during 1997–2016, Earth System Science Data, 9, 697-720, 2017.

Wallington, T. J., Sehested, J., and Nielsen, O. J.: Atmospheric chemistry of CF3C (O) O2 radicals. Kinetics of their reaction with NO2 and kinetics of the thermal decomposition of the product CF3C (O) O2NO2, Chemical physics letters, 226, 563-569, 1994.

Wang, Y., Jacob, D. J., and Logan, J. A.: Global simulation of tropospheric O3-NO x-hydrocarbon chemistry: 1. Model formulation, Journal of Geophysical Research: Atmospheres, 103, 10713-10725, 1998.

Weng, H., Lin, J., Martin, R., Millet, D. B., Jaeglé, L., Ridley, D., Keller, C., Li, C., Du, M., and Meng, J.: Global high-resolution emissions of soil NOx, sea salt aerosols, and biogenic volatile organic compounds, Scientific Data, 7, 148, 2020.

Wesely, M.: Parameterization of surface resistances to gaseous dry deposition in regional-scale numerical models, Atmospheric Environment, 41, 52-63, 2007.

Williams, A. J., Grulke, C. M., Edwards, J., McEachran, A. D., Mansouri, K., Baker, N. C., Patlewicz, G., Shah, I., Wambaugh, J. F., Judson, R. S., and Richard, A. M.: The CompTox Chemistry Dashboard: a community data resource for environmental chemistry, J Cheminform, 9, 61, 10.1186/s13321-017-0247-6, 2017.

Xiao, Y., Logan, J. A., Jacob, D. J., Hudman, R. C., Yantosca, R., and Blake, D. R.: Global budget of ethane and regional constraints on US sources, Journal of Geophysical Research: Atmospheres, 113, 2008.

Zender, C. S., Bian, H., and Newman, D.: Mineral Dust Entrainment and Deposition (DEAD) model: Description and 1990s dust climatology, Journal of Geophysical Research: Atmospheres, 108, 2003.